ACS OMEGA

http://pubs.acs.org/journal/acsodf

Article

Efficient Perovskite Solar Cells via Phenethylamine Iodide Cation-Modified Hole Transport Layer/Perovskite Interface

Ching-Ho Tien, Wei-Cheng Lin, and Lung-Chien Chen*

Cite This: *ACS Omega* 2022, 7, 37359−37368

Read Online

ACCESS | Metrics & More | Article Recommendations | Supporting Information

ABSTRACT: Perovskite solar cells (PeSCs) were fabricated by using $Cs_xFA_{1-x}PbI_{3-x}Cl_x$ as the photoactive layer, and the effects of different proportions of cesium chloride (CsCl)/formamidinium iodide on perovskites were investigated. Cesium (Cs) can stabilize the α phase of the perovskite, while chlorine (Cl) can increase the size and crystallinity of perovskite crystals and reduce non-radiative cladding, thereby improving the performance of the overall device. The maximum power conversion efficiency (PCE) measured for $Cs_{0.2}FA_{0.8}PbI_{2.8}Cl_{0.2}$-based PeSCs was 18.9%. To further improve the photovoltaic characteristics of PeSCs, $Cs_{0.2}FA_{0.8}PbI_{2.8}Cl_{0.2}$-based PeSCs were introduced into different concentrations of phenethylammonium iodide (PEAI) to modify the interface between the NiO_x hole transport layer (HTL) and the perovskite photoactive layer, which can simultaneously promote excellent crystallinity of the perovskite layer and passivated interfacial defects, reducing recombination near the perovskite/HTL interface in PeSCs, thereby increasing the efficiency of the device. Compared with the control $Cs_{0.2}FA_{0.8}PbI_{2.8}Cl_{0.2}$-based PeSC, the PCE of PeSC with the PEAI (10 mg/mL)-modified NiO_x/perovskite interface increased significantly from 18.9 to 20.2%.

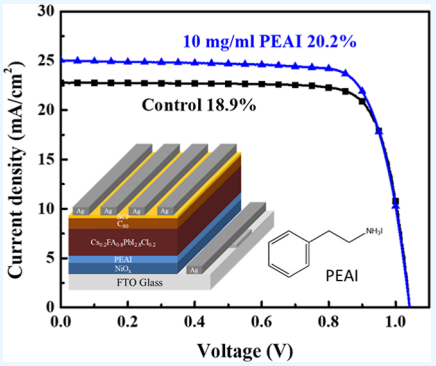

1. INTRODUCTION

As a novel solar photovoltaic device, the power conversion efficiency (PCE) of lead-based halide perovskite (LHP) solar cells (PeSCs) have increased from the initial 3.8 to 25.7%.[1−3] Although great achievements have been made, some significant challenges remain, including reproducibility and environment stability. LHP films can be prepared by conventional low-temperature solution methods. Due to its low formation energy, defects were easily generated in the interior, surface, and grain boundaries of the films, which will trap photogenerated charges, resulting in non-radiative recombination energy loss. It also accelerates the degradation process of the device, limiting the open-circuit voltage and overall performance of the device.[4] Although LHP has demonstrated its own high-defect tolerance,[5] these defects also affect the energy band matching between the LHP photoactive layer and the corresponding carrier transport layer.[6,7] In addition, vacancy defects caused by ion migration can also cause hysteresis in the forward and reverse scanning of the device,[8] and a large amount of ion migration can also lead to material degradation.[9] Therefore, reducing or passivating these defects were crucial for fabricating efficient PeSCs. To reduce surface/internal defects in LHP films, various modification/passivation methods have been proposed, including the use of modified preparation processes,[10,11] additive doping,[12,13] component engineering,[14,15] solvent processes,[16,17] and interface modification passivation,[18,19] which can reduce the density of defect states of LHPs. Among these techniques, interfacial modification/passivation engineering is a widely used and very effective method for defect reduction. This method could add a suitable modification/passivation layer between the transport layer/LHP photoactive layer or the transport layer/electrode, and the following improvements were usually achieved: (1) adjust the energy-level matching between the interfaces, reduce the charge transport barrier, and improve the charge transport capacity; (2) it can effectively control the LHP nucleation and grain growth, and by preparing large grains to reduce the channels of defects in grain boundaries and internal grains to achieve the purpose of self-passivation; (3) the designed modified layer containing hydrophobic groups can effectively prevent the intrusion of water vapor, and an organic molecular modification layer containing the Lewis base or Lewis acid functional group can passivate/modify the defects caused by insufficient coordination of metal cations and halide anions of LHP, respectively; (4) the introduction of 2D materials on the surface of three-dimensional (3D) LHPs to form mixed-dimensional LHPs can not only passivate defects on the LHP surface but also use the hydrophobic characteristics of 2D LHPs to prevent the intrusion of moisture in the air, thereby improving the stability of LHP to humidity. Among them,

Received: June 25, 2022
Accepted: October 3, 2022
Published: October 14, 2022

https://doi.org/10.1021/acsomega.2c03976
ACS Omega 2022, 7, 37359−37368

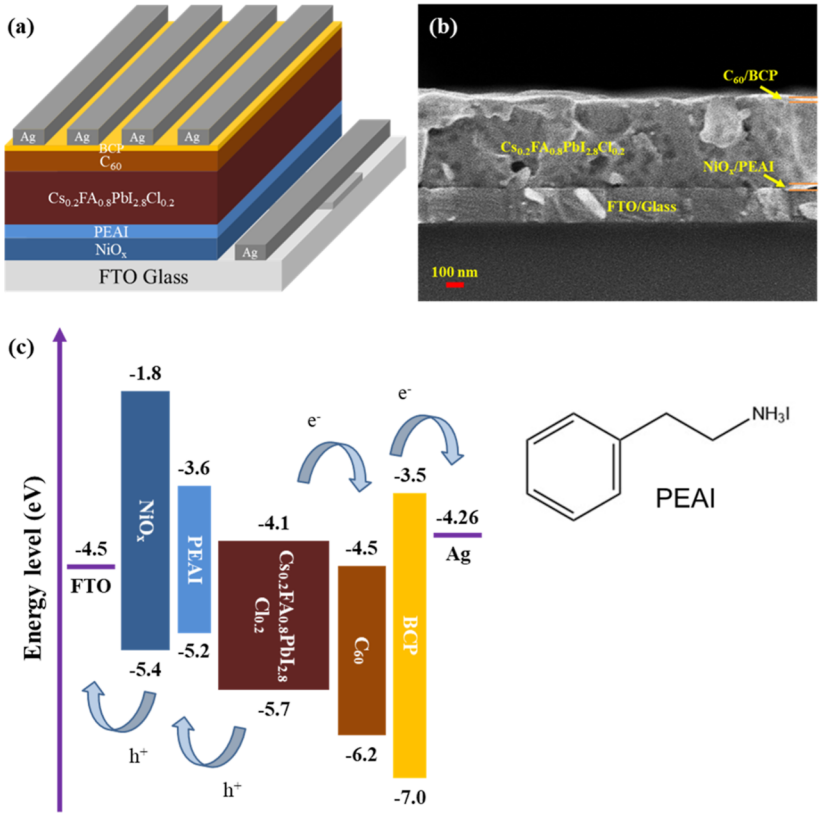

Figure 1. Schematic illustration of the (a) LHP solar cell configuration, (b) cross-sectional SEM image, and (c) energy-level alignment. Inset shows the chemical structure of the PEAI.

organic ammonium halide salts, such as phenethylammonium iodide (PEAI), have been successfully used to passivate LHP grain boundaries and surface, improve the photovoltaic performance of the PeSCs, and obtained more than 25% efficiency certification value.[20−24] Degani et al.[22] also proposed the PEAI dual-interface modification method and the incorporation of ionic liquids into the LHP photoactive layer, thereby making the device both efficient and stable, with a maximum PCE of 23.7%.

In PeSCs, $FAPbI_3$ as an ideal LHP material has the narrower band gap of 1.48 eV and the broader optical absorption range compared to $MAPbI_3$ (1.57 eV), which was able to reach the theoretical PCE of PeSCs.[25,26] However, the LHP black phase (α-phase) of photoactive $FAPbI_3$ was thermodynamically stable only above 150 °C, which readily degrades to the non-photoactive LHP yellow δ-phase at room temperature. This makes $FAPbI_3$-based PeSCs challenging for practical applications.[27−30] Studies have shown that photoactive α-$FAPbI_3$ LHPs can inhibit the phase transformation by partially incorporating mixed cations such as methylammonium (MA^+), cesium (Cs^+), rubidium (Rb^+), guanidinium (Gu^+), potassium (K^+), and other cations into $FAPbI_3$.[14,31−40] In particular, the incorporation of Cs^+ can effectively achieve better stability of the α-$FAPbI_3$ LHP structure, which was attributed to the lattice contraction caused by the interaction of FA^+, I^-,[41,42] and entropic stabilization.[43] Recently, we found that the addition of chloride anion (Cl^-) could improve the crystallinity, grain size, PCE efficiency, and α-phase stability of $FAPbI_3$-based PeSCs.[12,31,39,40,44−48] Pham et al.[44] reported that the addition of CsCl/MACl effectively stabilized the structure, morphology, crystallinity, and grain size of cubic supercell $FAPbI_3$, thereby enhancing the carrier lifetime. The optimized PeSC with 10 mol % CsCl exhibited the best PCE of 21.98%.

In this work, $Cs_xFA_{1-x}PbI_{3-x}Cl_x$ LHPs with different proportions of cesium chloride (CsCl)/formamidinium iodide (FAI) were synthesized to reveal the influences on the morphological, structural stability, and optical properties. This approach effectively increases the grain size and film quality, thereby improving the charge mobility and reducing the non-radiative carrier recombination at grain boundaries. In consequence, we achieved a PeSC PCE of 18.9% for a LHP film made with an optimal CsCl/FAI (0.2/0.8) composition ratio. Moreover, in order to improve the device efficiency and stability of PeSCs, by introducing PEAI to modify the NiO_x/LHPs interface, a high-quality LHP and passivating interface defects were obtained, promoting carrier transport and extraction abilities. The PEAI-treated $Cs_{0.2}FA_{0.8}PbI_{2.8}Cl_{0.2}$ PeSC exhibited PCE enhancements ranging from 18.9 to 20.2% and superior stability compared to control $Cs_{0.2}FA_{0.8}PbI_{2.8}Cl_{0.2}$ PeSC.

2. EXPERIMENTAL SECTION

2.1. Materials. Cesium chloride (CsCl, 99.99%), lead iodide (PbI_2, 99.9985%), nickel(II) formate dihydrate, ethylenediamine (99%), ethanolamine (98%), ethylene glycol (99%), and bathocuproine (BCP, 98%)) were purchased from Alfa Aesar. Formamidinium iodide (FAI) and phenethylammonium iodide (PEAI) were purchased from FrontMaterials. Dimethyl sulfoxide (DMSO, 99.9%), *N*,*N*-dimethyl formamide (DMF, 99.8%), and fullerene (C_{60}, 99.95%) were purchased from Uni-Onward. The patterned FTO-coated glass substrate (7 Ω sq^{-1}) was purchased from Ruilong.

https://doi.org/10.1021/acsomega.2c03976
ACS Omega 2022, 7, 37359−37368

2.2. Materials Fabrication. To prepare the NiO_x precursor, 932 mg (6.27 mmol) of nickel formate dihydrate with 0.668 mL of ethylenediamine and 0.603 mL of ethanolamine was dissolved in 10 mL of ethylene glycol string at 60 °C for 2 h and then stirred for 24 h at room temperature. The PEAI solutions were prepared by dissolving PEAI in IPA solvent with different concentrations of 5, 10, 15, and 20 mg/mL. CsCl was combined with FAI at different proportions (CsCl/FAI = 0.05/0.95, 0.1/0.9, 0.15/0.85, 0.2/0.8, and 0.25/0.75) to obtain mixed $Cs_xFA_{1-x}PbI_{3-x}Cl_x$ halide LHPs. For a stoichiometric ratio of CsCl/FAI = 0.2/0.8, the 1 M precursor solution of $Cs_{0.2}FA_{0.8}PbI_{2.8}Cl_{0.2}$ LHP was prepared by dissolving PbI_2 (1 mmole; 461.01 mg), FAI (1 mmole; 137.58 mg), and CsCl (0.2 mmole; 33.67 mg) in 1 mL of anhydrous DMF/DMSO (4/1 vol/vol) at room temperature of 25 °C for about 24 h.

2.3. Solar Cell Fabrication. FTO-coated glass substrates were cleaned sequentially with acetone, ethanol, and isopropanol for 15 min in an ultrasonic cleaner, followed by drying and 15 min ultraviolet ozone treatment. The NiO_x precursor was spin-coated onto a patterned FTO-coated glass at 4500 rpm for 90 s and annealed at 120 °C for 10 min on a hot plate in air, followed by baking in an oven at 350 °C for 10 min. The 50 μL PEAI solution was spin-coated onto the NiO_x hole transport layer (HTL) at 5000 rpm for 30 s to form a modified layer and transferred into a nitrogen-filled glovebox. Thereafter, a two-step method at 1000 rpm for 10 s and 5000 rpm for 40 s of 80 μL of LHP precursor solution was used to deposit the LHP film on pure NiO_x or PEAI-modified NiO_x layers, respectively. Toluene (100 μL) was used as an antisolvent and dropped on the spinning film 20 s prior to the end of the second step. After deposition, the substrate was annealed at 100 °C for 10 min on a hot plate to form a $Cs_{0.2}FA_{0.8}PbI_{2.8}Cl_{0.2}$ LHP film. Subsequently, the 20 nm-thick C_{60} electron transport layer and 5 nm-thick BCP electron blocking layer were sequentially deposited onto the LHP film under high vacuum. Finally, 100 nm-thick Ag was thermally evaporated on the top of PeSCs to form the top electrode, as shown in Figure 1a. The structure of the PEAI-modified PeSC is shown in the cross-sectional scanning electron microscopy (SEM) image in Figure 1b, in which the PEAI-modified NiO_x layer was about 30−40 nm and the $Cs_{0.2}FA_{0.8}PbI_{2.8}Cl_{0.2}$ LHP layer thickness was determined to be ≈500 nm. The energy band diagram of the PeSC and the charge transport behavior occurring in the PEAI-modified NiO_x layer were shown in Figure 1c. The PEAI-modified interlayer can significantly alleviate the lattice mismatch between NiO_x and LHP, thereby suppressing the formation of interfacial defects, promoting high-quality crystal nucleation and growth of LHP films, and improving the PCE and stability of inverted planar PeSC.

2.4. Characterization. Optical absorption and photoluminescence (PL) spectra of the LHP films were conducted using a UV−Visible−Near Infrared (UV/VIS/NIR) spectrophotometer (V-770, Jasco, Japan) and a fluorescence spectrophotometer (F-7000, Hitachi, Japan). The lasing spectra and carrier lifetime were studied using an imaging spectrometer (iHR320, Horiba Jobin Yvon, France), where a 375 nm pulsed laser was used as the pumping laser. The phases and crystallinity of the LHP films were characterized by a X-ray diffractometer (X'Pert PRO MRD, PANalytical, the Netherlands). The surface morphologies of the LHP films and the cross-sectional structure of PeSC were taken using a field-emission SEM (FESEM, Sigma, ZEISS, Germany). The $J-V$ curves of PeSC photovoltaic properties were recorded using a Keithley 2420 sourcemeter with a solar simulator (MFS-PV-Basic, Hong-Ming Technology Co., Ltd., Taiwan) under illumination of air-mass (AM) 1.5 G standard sunlight at 100 mW cm^{-2}, calibrated with an NREL standard silicon reference cell (PVM-894, PV Measurements Inc., USA). The photoactive area of PeSC was 0.04 cm^2. The external quantum efficiency (EQE) was tested using a QE measurement system (LSQE-R, LiveStrong Optoelectronics Co., Ltd., Taiwan) equipped with a UV−vis−NIR spectrophotometer (LAMBDA 35, PerkinElmer, USA) and a 150 W xenon lamp (XES-204S, San-Ei Electric Co., Ltd., Japan) as a light source.

3. RESULTS AND DISCUSSION

The X-ray diffraction (XRD) patterns of the LHP films depending on the CsCl/FAI proportions are shown in Figure 2. Figure S1 depicts the XRD patterns of the pure $FAPbI_3$ and

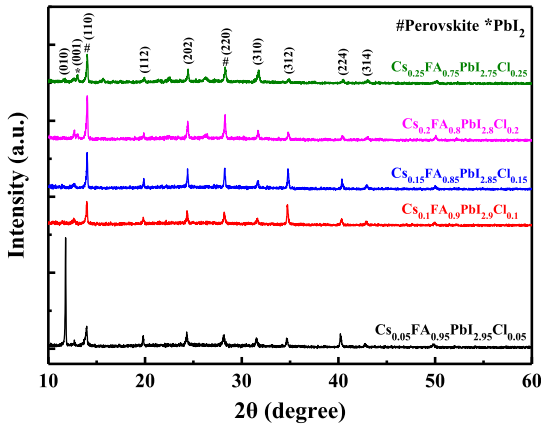

Figure 2. XRD patterns of the LHP films with different proportions of CsCl/FAI.

pure $CsPbCl_3$ LHP films. The pure $FAPbI_3$ LHP film annealed at 100 °C had its characteristic peak at 2θ = 11.54°, corresponding to the d-hexagonal phase.[49] The diffraction peaks at 22.22 and 45.49° of pure $CsPbCl_3$ LHP films correspond to their (110) and (220) planes, which resemble with the cubic phase of $CsPbCl_3$ [JCPDS no. 18#0366]. Two dominant peaks of LHPs were located at around 14 and 28°, originating from the (110) and (220) planes of the 3D LHP phase, respectively. As the CsCl/FAI proportion increases, the δ-phase peak gradually decreased, which enhanced the diffraction intensities of the (110) and (220) peaks. At the same time, the full width at half-maximum (FWHM) of the (110) peak was narrowed, and the (001) plane of the PbI_2 phase becomes weaker, indicating that the as-prepared films were completely converted into stable α-LHP and enhanced crystallinity. It was evident that the $Cs_{0.2}FA_{0.8}PbI_{2.8}Cl_{0.2}$ LHP with a CsCl/FAI proportion of 0.2/0.8 obtains the highest (110) peak intensity and narrow FWHM, indicating its enhanced crystallinity and larger grain size. The CsCl/FAI proportion was further increased to 0.25/0.75, the FWHM of $Cs_{0.25}FA_{0.75}PbI_{2.75}Cl_{0.25}$ LHP was no longer narrowed, and the peak intensity tended to decrease. This indicates that too much CsCl can neither further increase the grain size nor enhance the crystallinity. When the CsCl/FAI proportion was 0.05/0.95, the $Cs_{0.05}FA_{0.95}PbI_{2.95}Cl_{0.05}$ LHP film showed a δ-phase peak at 11.8° and a PbI_2 peak (12.7°). Normally, to obtain stable α-$FAPbI_3$ LHPs, an annealing temperature higher than

https://doi.org/10.1021/acsomega.2c03976
ACS Omega 2022, 7, 37359−37368

150 °C was required.[33,40,46]. Due to the low proportion of CsCl and the low annealing temperature of 100 °C (all samples in this experiment were annealed at 100 °C), the crystallization temperature was insufficient to form stable α-$FAPbI_3$, resulting in the degradation of the $Cs_{0.05}FA_{0.95}PbI_{2.95}Cl_{0.05}$ LHP film into a poor δ-phase.

The SEM surface morphologies and size distribution charts of the obtained LHP films with different CsCl/FAI proportions were further analyzed, as shown in Figures 3 and

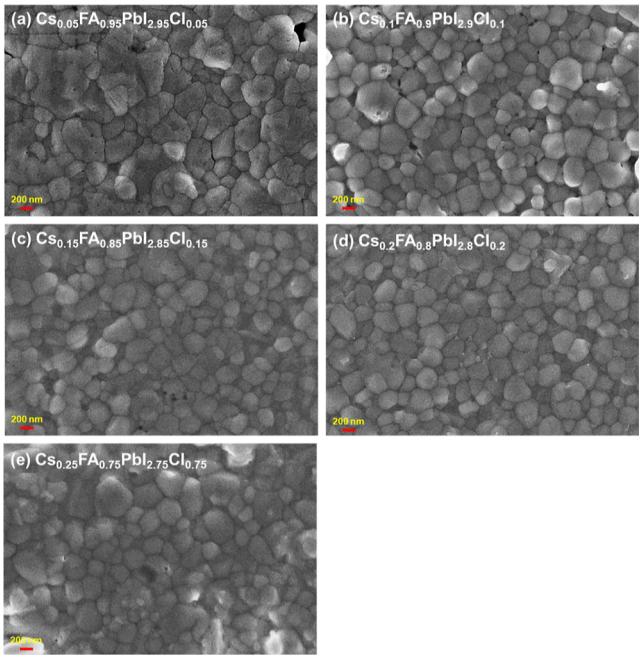

Figure 3. (a–e) Top view SEM images of the LHP films with different proportions of CsCl/FAI.

S2. It can be observed that the grain size of the LHP not only increases with the increase of the CsCl/FAI proportions but also reduces the defects and pores. Among them, the $Cs_{0.2}FA_{0.8}PbI_{2.8}Cl_{0.2}$ LHP film with the CsCl/FAI proportion of 0.2/0.8 obtained a denser and more uniform surface morphology. When the CsCl/FAI proportion was increased to 0.25/0.75, it can be found that the grain size becomes smaller and the grain boundaries become more, showing a poorer surface morphology. The average particle sizes of $Cs_{0.05}FA_{0.95}PbI_{2.95}Cl_{0.05}$, $Cs_{0.1}FA_{0.9}PbI_{2.9}Cl_{0.1}$, $Cs_{0.15}FA_{0.85}PbI_{2.85}Cl_{0.15}$, $Cs_{0.2}FA_{0.8}PbI_{2.8}Cl_{0.2}$, and $Cs_{0.25}FA_{0.75}PbI_{2.75}Cl_{0.25}$ LHPs were 327, 202.9, 180.8, 140.5, and 128.2 nm, respectively.

Figure 4a shows the UV–vis absorption spectra of LHP films with different proportions of CsCl/FAI. Affected by the structural instability, although the $Cs_{0.05}FA_{0.95}PbI_{2.95}Cl_{0.05}$ LHP film has better optical absorbance property, the XRD shows that the as-prepared LHP film was δ-phase and does not form a photoactive phase. For the CsCl/FAI proportions from 0.1/0.9 to 0.2/0.8, it can be seen that the optical absorbance of the LHP films obtains more light and a slightly blue shift, which should be beneficial to improve the solar cell performance, where the $Cs_{0.2}FA_{0.8}PbI_{2.8}Cl_{0.2}$ LHP film had the best optical absorbance. However, the use of $Cs_{0.25}FA_{0.75}PbI_{2.75}Cl_{0.25}$ LHP film with a CsCl/FAI ratio of 0.25/0.75 weakens the light absorption, resulting in a decrease in crystallinity due to the substitution of FA by Cs. The PL spectra of the LHP films with different proportions of CsCl/FAI are shown in Figure 4b. The PL emission peak exhibits a blue shift with increasing CsCl/FAI proportions due to FA^+ ion substitution, which was consistent with the absorption spectra. In addition, the $Cs_{0.2}FA_{0.8}PbI_{2.8}Cl_{0.2}$ LHP film with a CsCl/FAI ratio of 0.2/0.8 had the highest PL emission peak intensity (the peak was ca. 778 nm), which proves that there were fewer internal traps, better crystallinity, and slower charge recombination rate. To quantitatively analyze the carrier lifetime, biexponential decay model was used to fit the PL decay curves, where a fast and a slow component trace fitted with function: $I(t) = A_1 \exp(-t/\tau_1) + A_2 \exp(-t/\tau_2)$. The fitting parameters of time-resolved PL curves are shown in Figure 4c and listed in Table S1. We found that the $Cs_{0.2}FA_{0.8}PbI_{2.8}Cl_{0.2}$ LHP film with a CsCl/FAI ratio of 0.2/0.8 exhibits the longest PL lifetime (160.4 ns) as compared with other compositions, suggesting the retarded charge recombination inside the film.

To investigate the exact effect of different CsCl/FAI proportions on the photovoltaic performance of PeSCs, 30 PeSCs were fabricated. As shown in Figure 5, the statistical results of photovoltaic parameters of PeSCs with different CsCl/FAI proportions were counted. Figure 6 shows the J–V curves of the best PeSC for each case, and the corresponding photovoltaic performance parameters are summarized in Table S2. From the statistical count of photovoltaic parameters, it can be seen that as the CsCl/FAI proportions increases, the average J_{sc}, FF, and PCE of the PeSCs under each case increase significantly, whereas V_{oc} does not increase significantly. Therefore, the overall short-circuit current density (J_{sc}), fill factor (FF), and PCE of $Cs_{0.2}FA_{0.8}PbI_{2.8}Cl_{0.2}$ PeSC based on a CsCl/FAI proportion of 0.2/0.8 were higher than those of other conditional PeSCs. This indicates that the introduction of CsCl was believed to play an important role in improving the photovoltaic parameters. Based on the champion, $Cs_{0.2}FA_{0.8}PbI_{2.8}Cl_{0.2}$ PeSC had the best photovoltaic properties, it yields a PCE of 18.9% with a J_{sc} of 22.7 mA cm^{-2}, a V_{oc} of 1.04 V, and a FF of 79.8%. This was attributed to the better crystallinity, suitable grain size, and better optical properties of the $Cs_{0.2}FA_{0.8}PbI_{2.8}Cl_{0.2}$ LHP film, which could more effectively separate electrons/holes and reduce non-radiative recombination. However, PeSCs with CsCl/FAI ratios of 0.05/0.95 and 0.25/0.75 have poor photovoltaic properties, mainly due to the appearance of δ-phase (small amount of CsCl) and smaller grain size (redundant CsCl), respectively, resulting in poor crystallinity and optical properties, as well as suppressing charge carrier transport.

Based on $Cs_{0.2}FA_{0.8}PbI_{2.8}Cl_{0.2}$, the LHP film had a larger grain size, a better crystallinity, and a higher absorbance, resulting in better performance efficiency. The LHP film (control) prepared at this proportion (CsCl/FAI = 0.2/0.8) was selected for the device interface passivation strategy to further improve the performance efficiency. Deposition of PEAI between NiO_x and LHP films to passivate the interface helps to form high-quality LHPs and prepare large-grained LHPs. Figure 7 presents the XRD patterns of LHP films modified with various PEAI solution concentrations. The (110), (203), (220), and (310) crystal planes of all LHP films correspond to the diffraction peaks of 14.0, 24.4, 28.2, and 31.7°, respectively. Compared with the control LHP film, the diffraction peak intensities of the (110) and (220) planes of the PEAI-modified LHP film were significantly enhanced, indicating better crystallization and the larger grain sizes of the LHP film. The PEAI-modified LHP film with a PEAI

https://doi.org/10.1021/acsomega.2c03976
ACS Omega 2022, 7, 37359–37368

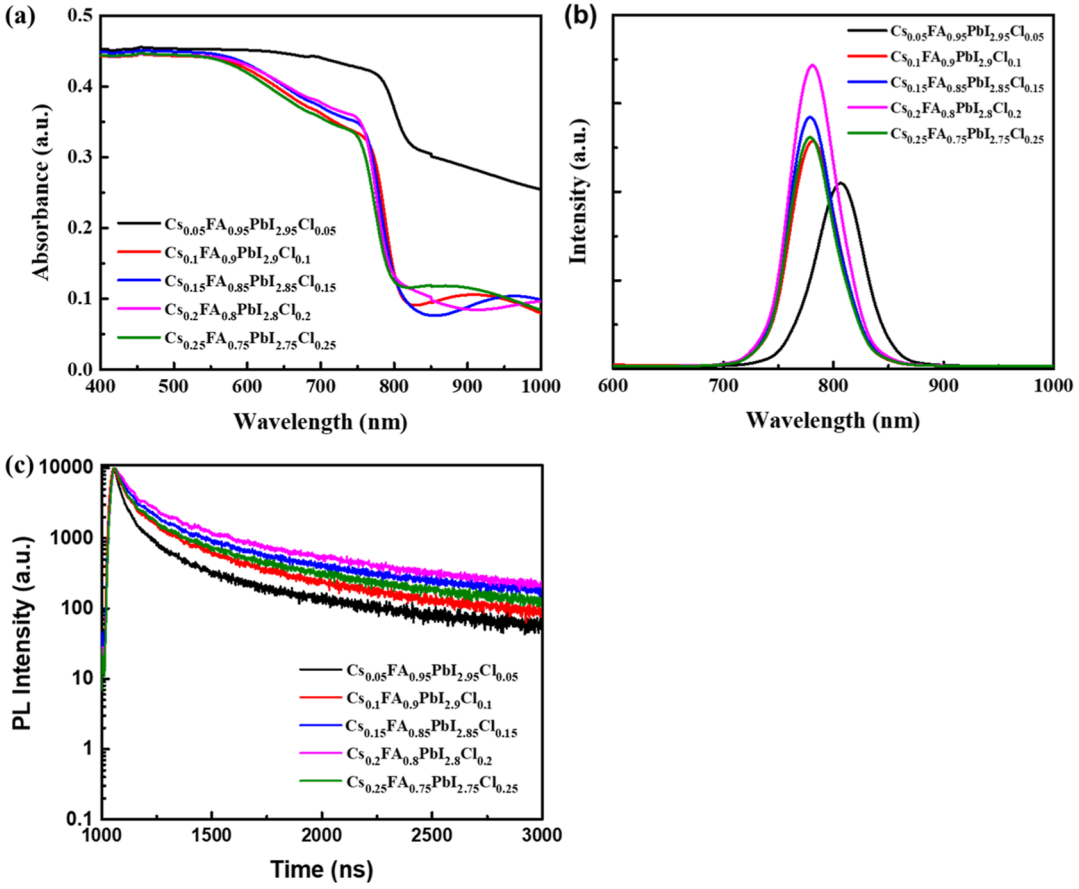

Figure 4. (a) Absorption, (b) PL, and (c) time-resolved PL spectra of the LHP films with different proportions of CsCl/FAI.

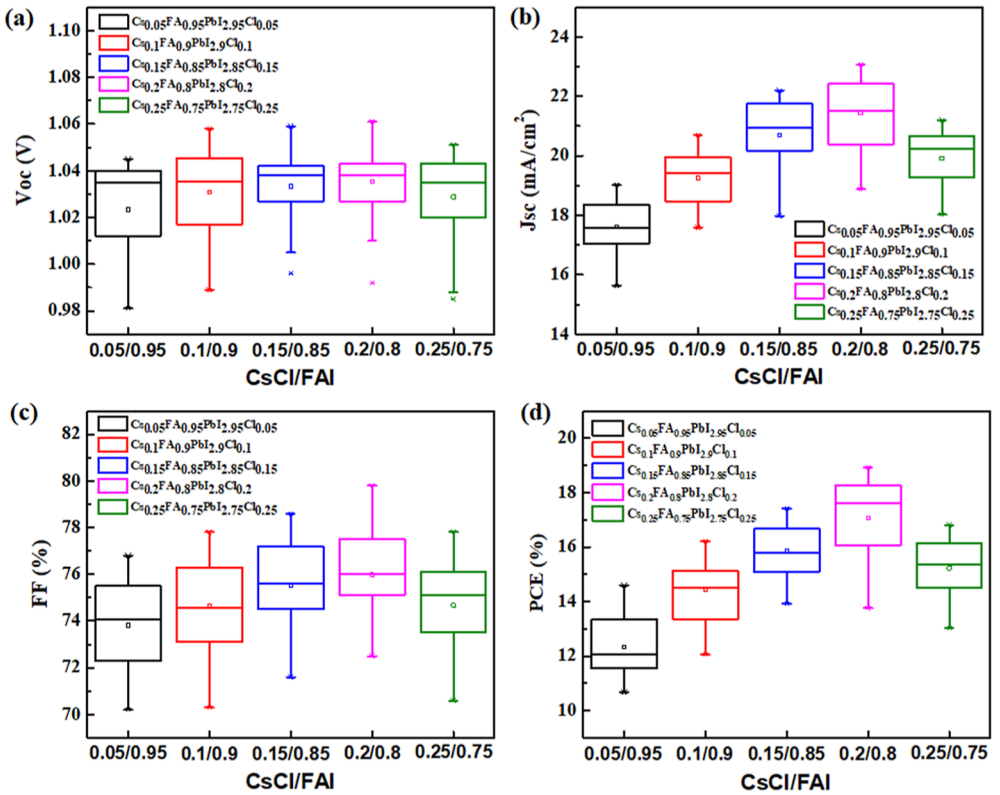

Figure 5. Statistical data of (a) V_{oc}, (b) J_{sc}, (c) FF, and (d) PCE for PeSCs prepared with different proportions of CsCl/FAI.

https://doi.org/10.1021/acsomega.2c03976
ACS Omega 2022, 7, 37359−37368

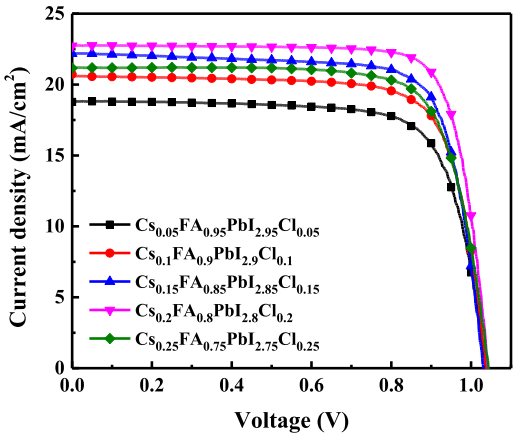

Figure 6. Typical $J-V$ curves of PeSCs prepared with different proportions of CsCl/FAI.

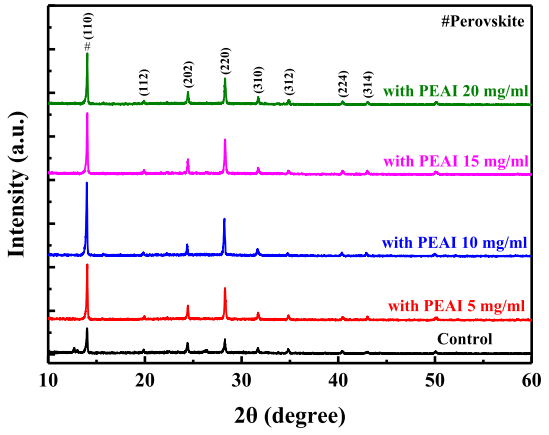

Figure 7. XRD patterns of the LHP films modified with various PEAI solution concentrations.

concentration of 10 mg/mL and the diffraction peak of LHP crystal orientation (110) and (220) were the strongest, and other diffraction peaks were also significantly improved compared with other concentrations, indicating that it has the best crystallization. When the PEAI concentration increased to 15 and 20 mg/mL, the diffraction peak of its LHP crystal phase (110) decreased, which may be caused by excessive organic cation PEA^+.

The enhanced crystallization of LHP films based on the introduction of PEAI was confirmed by the XRD characteristics. This inference was intuitively reflected in SEM images. Figure 8 shows the SEM surface morphology of LHP films modified with various PEAI solution concentrations. It can be found that PEAI-modified LHP films exhibit enlarged grain films at a PEAI concentration of 10 mg/mL. However, as the concentration was 15 and 20 mg/mL, the crystallinity of LHPs was not better, mainly because too much organic cations (PEA^+) in PEAI leads to more surface defects. Therefore, spin-coating a layer of PEAI with a suitable concentration between NiO_x and LHPs can obtain high crystallinity and high-quality LHP films, which can reduce defects and facilitate the preparation of efficient PeSCs.

Figure 9a measures the absorption spectra of LHP films modified with various PEAI solution concentrations. At the absorption wavelength between 650 and 700 nm, when the PEAI concentration was from to 10 mg/mL, the optical

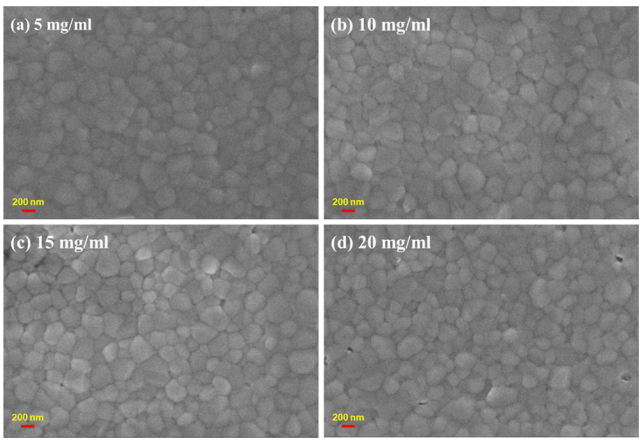

Figure 8. (a–d) Top view SEM images of the LHP films modified with various PEAI solution concentrations.

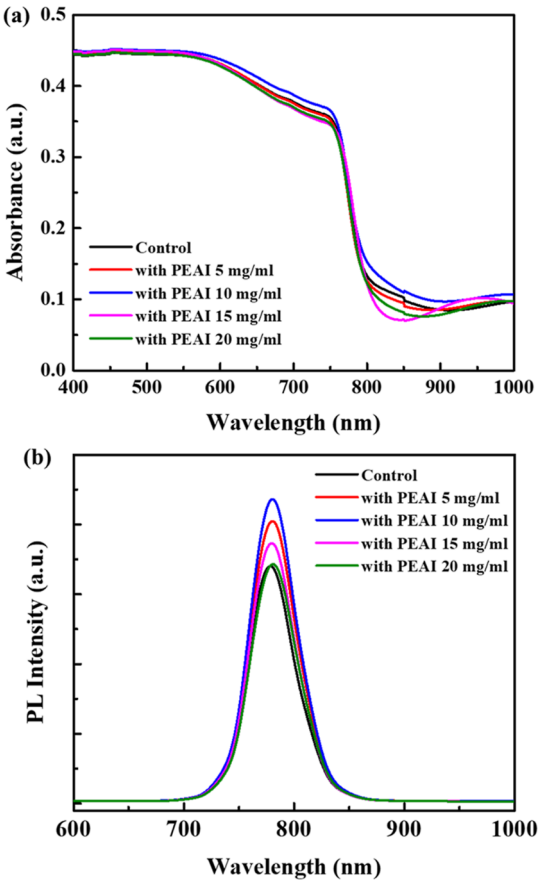

Figure 9. (a) Absorption and (b) PL spectra of the LHP films modified with various PEAI solution concentrations.

absorption increasingly enhanced, mainly based on the increased crystallinity and grain size of the LHP film, with fewer surface defects, which could improve the J_{sc} of PeSCs. The best optical absorbance was obtained at a solution concentration of 10 mg/mL of PEAI. However, when the PEAI concentration was increased to 15 and 20 mg/mL, due to excessive PEA^+ organic cations, the optical absorbance decreased, which in turn reduced the photovoltaic properties of PeSCs. Figure 9b shows the PL spectra of the LHP films modified with various concentrations of PEAI solutions, which were consistent with the absorption spectra analysis, and their

https://doi.org/10.1021/acsomega.2c03976
ACS Omega 2022, 7, 37359−37368

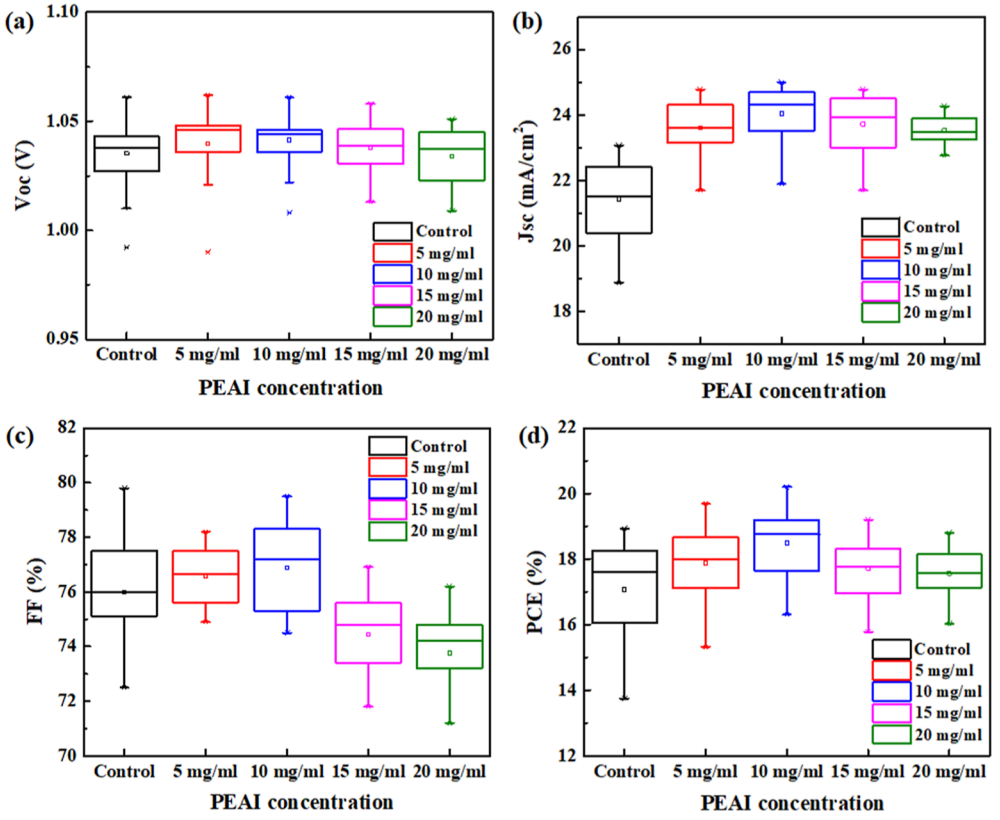

Figure 10. Statistical data of (a) V_{oc}, (b) J_{sc}, (c) FF, and (d) PCE for PeSCs modified with various PEAI solution concentrations.

peaks were located around 778 nm. When the PEAI concentration was 10 mg/mL, the PL peak intensity was the strongest, indicating that its LHP film has better crystallinity and fewer defects and pores, which has been confirmed by XRD and SEM.

Figure 10 explores the dependence of the performance of PEAI-modified PeSCs on PEAI concentration, in which J_{sc} significantly increased after PEAI treatment, its PCE was higher than that of control PeSC, and the best performance was obtained at a solution concentration of 10 mg/mL. The effect of PEAI solution concentration on $J-V$ curves of best-performing PeSCs for each case is exhibited in Figure 11, and the corresponding photovoltaic parameters are listed in Table S3. Overall, PEAI at a solution concentration of 10 mg/mL

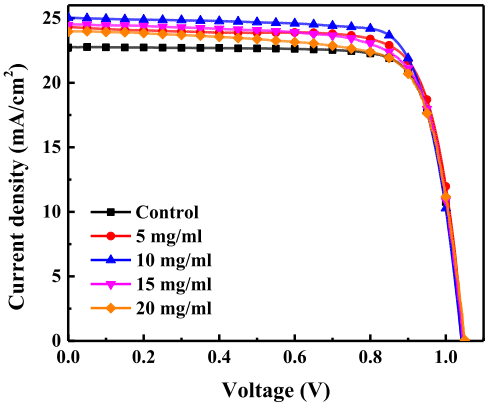

Figure 11. Typical $J-V$ curves of PeSCs modified with various PEAI solution concentrations.

appeared to be the best choice for the best photovoltaic performance, exhibiting a PCE of 20.2%, a J_{sc} of 25 mA cm^{-2}, a V_{oc} of 1.04 V, and a FF of 77.5%. PEAI-modified LHP films with large grain size, high crystallinity, and high optical absorbance achieve high performance. It was also noted that the PEAI modification especially enhances the J_{sc} and FF of PeSC by improving the NiO_x/LHP interface contact properties, passivating surface defects and favoring carrier transport. However, when the concentration was 15 and 20 mg/mL, the surface passivation layer formed due to the excess organic cation PEA^+ increased with the increase of the concentration. Therefore, the formed thicker PEAI layer may increase the resistance due to the enhanced insulating properties, leading to low FF and degrading the photovoltaic performances of PeSCs. A comparison of the Cs and Cl-treated CsFA-based PeSCs considered in other works is given in Table 1. It could be found that the performance of CsCl and PEAI-treated CsFA-based PeSCs in this study is still on par with other works due to the different overall PeSC device structures.

Modification/passivation of the interface between NiO_x HTL and LHP photoactive layer using PEAI could improve the crystallinity and optical absorbance, which improve the J_{sc} of PeSCs from 22.7 to 25 mA cm^{-2}. In addition, the EQE of PEAI-modified PeSC was significantly improved between 350 and 750 nm, as shown in Figure 12a, indicating that PEAI modification not only improves LHP layer crystallinity, reduces carrier recombination, but also improves carrier transport and extraction abilities. As shown in Figure 12b, after 168 h of storage in nitrogen, the control and PEAI-modified PeSCs maintained 86 and 76% of their initial efficiencies, respectively, demonstrating that the introduction of PEAI modification could effectively improve their stability.

https://doi.org/10.1021/acsomega.2c03976
ACS Omega 2022, 7, 37359−37368

Table 1. Performance Summary of Cs and Cl-Treated CsFA-Based PeSCs

materials	perovskite	J_{sc} (mA cm^{-2})	V_{oc} (V)	FF (%)	PCE (%)	ref
CsCl	$Cs_xFA_{1-x}PbI_3$	22.81	1.118	76.4	19.20	45 (2019)
CsCl	$Cs_{0.20}FA_{0.80}PbI_3$-(Cl)	24.10	1.10	77.6	20.6	46 (2019)
CsCl	$Cs_xFA_{1-x}PbI_3$	23.85	1.09	79.0	20.59	48 (2020)
CsCl	$Cs_xFA_{1-x}PbI_3$	24.93	1.112	79.3	21.98	44 (2021)
$PbCl_2$, BASCN	$Cs_{0.1}FA_{0.9}Pb(I_{0.9}Br_{0.1})_3$	22.6	1.09	77.6	19.12	50 (2022)
MACl, BASCN	$Cs_{0.1}FA_{0.9}Pb(I_{0.9}Br_{0.1})_3$	23.1	1.17	82.5	23.0	50 (2022)
CsCl, PEAI	$Cs_{0.2}FA_{0.8}PbI_{2.8}Cl_{0.2}$	25.0	1.04	77.5	20.20	his work

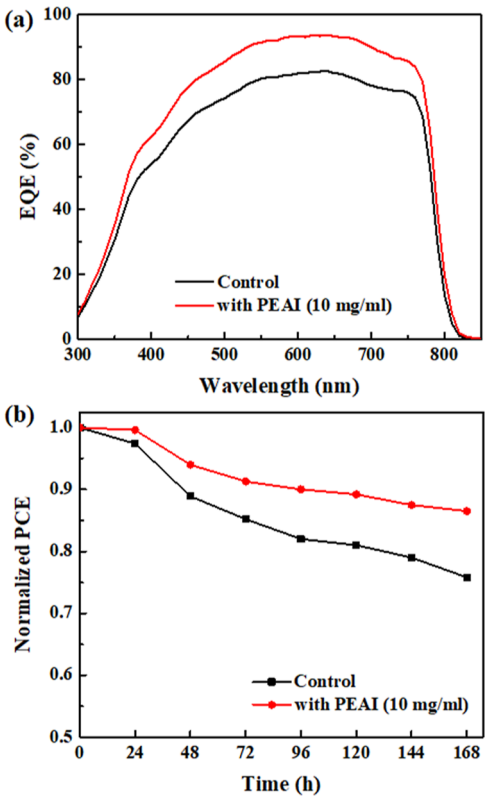

Figure 12. (a) EQE spectra and (b) normalized PCE stability evolution (N_2-filled glovebox) of PeSCs with and without PEAI treatment.

4. CONCLUSIONS

In conclusion, we developed a method for the preparation of LHP films via CsCl and FAI dual-organic cations and halogen anions. By using different CsCl/FAI proportions of CsCl/FAI, LHP films with different $Cs_xFA_{1-x}PbI_{3-x}Cl_x$ compositions were obtained. When CsCl/FAI was 0.2/0.8, the prepared $Cs_{0.2}FA_{0.8}PbI_{2.8}Cl_{0.2}$ LHP film had the best optical absorbance, the diffraction peak intensity of the LHP crystal phase (110) was the strongest, indicating the optimal crystallinity, and long PL carrier lifetime (160.4 ns), which could more effectively separate electrons/holes and reduce non-radiative recombination, achieving in 18.9% PeSC performance. To further improve the PCE of the PeSC, the deposition of PEAI on NiO_x facilitates to passivate defects of NiO_x and LHP interface, prevent carrier transport to the NiO_x/LHP interface, and improve the crystallinity, optical absorbance, and stability. PeSCs prepared with a concentration of 10 mg/mL PEAI coating displayed a PCE enhancement from 18.9 to 20.2% and a prolonged device lifetime. Under storage in a nitrogen glovebox for 168 h, a PEAI-modified PeSC retained 86% of its initial PCE. The implementation of PEAI was confirmed to be an effective modification/passivation strategy to boost the photovoltaic efficiency and stability of PeSCs.

■ ASSOCIATED CONTENT

Supporting Information

The Supporting Information is available free of charge at https://pubs.acs.org/doi/10.1021/acsomega.2c03976.

XRD patterns of the pure FAPbI3 and pure CsPbCl3 perovskite films; size distribution charts of the perovskite films with different proportions of CsCl/FAI, tables of TRPL and performance parameters of PeSCs prepared with different proportions of CsCl/FAI, and performance parameters of PeSCs modified with various PEAI solution concentrations (PDF)

■ AUTHOR INFORMATION

Corresponding Author

Lung-Chien Chen − *Department of Electro-Optical Engineering, National Taipei University of Technology, Taipei 10608, Taiwan;* orcid.org/0000-0001-5470-8491; Email: ocean@ntut.edu.tw

Authors

Ching-Ho Tien − *Department of Electronic Engineering, Lunghwa University of Science and Technology, Taoyuan 33306, Taiwan;* orcid.org/0000-0002-8731-5157

Wei-Cheng Lin − *Department of Electro-Optical Engineering, National Taipei University of Technology, Taipei 10608, Taiwan*

Complete contact information is available at: https://pubs.acs.org/10.1021/acsomega.2c03976

Author Contributions

L.-C.C. carried out the experiments, designed the study, and gave significant suggestions on writing the whole manuscript. C.-H.T. conceived the original idea, data analysis, and interpretation and wrote the manuscript. W.-C.L. prepared the samples and performed all measurements. All authors approved this manuscript.

Notes

The authors declare no competing financial interest.

■ ACKNOWLEDGMENTS

This research was supported by the National Science and Technology Council (Taiwan) under contract nos. 111-2221-E-027-040-MY3 and 111-2221-E-262-006.

REFERENCES

(1) Kojima, A.; Teshima, K.; Shirai, Y.; Miyasaka, T. Organometal halide perovskites as visible-light sensitizers for photovoltaic cells. *J. Am. Chem. Soc.* **2009**, *131*, 6050−6051.

(2) Kim, M.; Jeong, J.; Lu, H.; Lee, T. K.; Eickemeyer, F. T.; Liu, Y.; Choi, I. W.; Choi, S. J.; Jo, Y.; Kim, H. B.; Mo, S. I.; Kim, Y. K.; Lee, H.; An, N. G.; Cho, S.; Tress, W. R.; Zakeeruddin, S. M.; Hagfeldt, A.; Kim, J. Y.; Grätzel, M.; Kim, D. S. Conformal quantum dot-SnO_2 layers as electron transporters for efficient perovskite solar cells. *Science* **2022**, *375*, 302−306.

(3) Best Research-Cell Efficiencies. *National Renewable Energy Laboratory* https://www.nrel.gov/pv/assets/pdfs/best-research-cell-efficiencies-rev220126.pdf (Rev. Jan 26, 2022).

(4) Chen, B.; Rudd, P. N.; Yang, S.; Yuan, Y.; Huang, J. Imperfections and their passivation in halide perovskite solar cells. *Chem. Soc. Rev.* **2019**, *48*, 3842−3867.

(5) Saliba, M.; Matsui, T.; Domanski, K.; Seo, J. Y.; Ummadisingu, A.; Zakeeruddin, S. M.; Correa-Baena, J. P.; Tress, W. R.; Abate, A.; Hagfeldt, A.; Grätzel, M. Incorporation of rubidium cations into perovskite solar cells improves photovoltaic performance. *Science* **2016**, *354*, 206−209.

(6) Si, H.; Zhang, Z.; Liao, Q.; Zhang, G.; Ou, Y.; Zhang, S.; Wu, H.; Wu, J.; Kang, Z.; Zhang, Y. A-site management for highly crystalline perovskites. *Adv. Mater.* **2020**, *32*, 1904702.

(7) Lu, C. H.; Biesold-McGee, G. V.; Liu, Y.; Kang, Z.; Lin, Z. Doping and ion substitution in colloidal metal halide perovskite nanocrystals. *Chem. Soc. Rev.* **2020**, *49*, 4953−5007.

(8) Zhao, Y.; Liang, C.; Zhang, H.; Li, D.; Tian, D.; Li, G.; Jing, X.; Zhang, W.; Xiao, W.; Liu, Q.; Zhang, F. H. Z.; He, Z. Anomalously large interface charge in polarity-switchable photovoltaic devices: an indication of mobile ions in organic−inorganic halide perovskites. *Energy Environ. Sci.* **2015**, *8*, 1256−1260.

(9) Zhao, Y.; Zhou, W.; Ma, W.; Meng, S.; Li, H.; Wei, J.; Fu, R.; Liu, K.; Yu, D.; Zhao, Q. Correlations between immobilizing ions and suppressing hysteresis in perovskite solar cells. *ACS Energy Lett.* **2016**, *1*, 266−272.

(10) Liu, M.; Johnston, M. B.; Snaith, H. J. Efficient planar heterojunction perovskite solar cells by vapour deposition. *Nature* **2013**, *501*, 395−398.

(11) Chapagain, S.; Chandrasekhar, P. S.; McGott, D.; Bramante, R. C.; van Hest, M. F. A. M.; Reese, M. O.; Druffel, T.; Grapperhaus, C. A. Direct deposition of nonaqueous SnO_2 dispersion by blade coating on perovskites for the scalable fabrication of p−i−n perovskite solar cells. *ACS Appl. Energy Mater.* **2021**, *4*, 10477−10483.

(12) Ji, C.; Liang, C.; Zhang, H.; Sun, M.; Song, Q.; Sun, F.; Feng, X.; Liu, N.; Gong, H.; Li, D.; You, F.; He, Z. Secondary grain growth in organic−inorganic perovskite films with ethylamine hydrochloride additives for highly efficient solar cells. *ACS Appl. Mater. Interfaces* **2020**, *12*, 20026−20034.

(13) Lao, Y.; Wang, D.; Zhang, Z.; Zhang, Y.; Qu, B.; Xiao, L.; Chen, Z. Highly efficient perovskite solar cells enhanced by biphenyl-4,4-dithiol. *Sol. Energy Mater. Sol. Cells* **2022**, *235*, 111462.

(14) Jeon, N. J.; Noh, J. H.; Yang, W. S.; Kim, Y. C.; Ryu, S.; Seo, J.; Seok, S. I. Compositional engineering of perovskite materials for high-performance solar cells. *Nature* **2015**, *517*, 476−480.

(15) Badrooj, M.; Jamali-Sheini, F.; Torabi, N. Zn-doped Pb/Sn hybrid perovskite solar cells: Towards high photovoltaic performance. *Sol. Energy* **2022**, *236*, 63−74.

(16) Jeon, N. J.; Noh, J. H.; Kim, Y. C.; Yang, W. S.; Ryu, S.; Seok, S. I. Solvent engineering for high-performance inorganic−organic hybrid perovskite solar cells. *Nat. Mater.* **2014**, *13*, 897−903.

(17) Belay Adugna, G. B.; Yimer Abate, S. Y.; Tao, Y. T. High-efficiency and scalable solution-sheared perovskite solar cells using green solvents. *Chem. Eng. J.* **2022**, *437*, 135477.

(18) Seok, S. I.; Grätzel, M.; Park, N. G. Methodologies toward highly efficient perovskite solar cells. *Small* **2018**, *14*, 1704177.

(19) Malouangou, M. D.; Yang, Y.; Zhang, Y.; Bai, L.; Matondo, J. T.; Mbumba, M.; Akram, M. W.; Guli, M. Facilitate hole transport with thin 2D perovskite capping layer to passivate interface defects of 3D perovskite solar cells using PEABr. *Mater. Res. Bull.* **2022**, *150*, 111793.

(20) Jiang, Q.; Zhao, Y.; Zhang, X.; Yang, X.; Chen, Y.; Chu, Z.; Ye, Q.; Li, X.; Yin, Z.; You, J. Surface passivation of perovskite film for efficient solar cells. *Nat. Photonics 2019* **2019**, *13*, 460−466.

(21) Zhang, Y.; Jang, S.; Hwang, I. W.; Jung, Y. K.; Lee, B. R.; Kim, J. H.; Kim, K. H.; Park, S. H. Bilateral interface engineering for efficient and stable perovskite solar cells using phenylethylammonium iodide. *ACS Appl. Mater. Interfaces* **2020**, *12*, 24827−24836.

(22) Degani, M.; An, Q.; Albaladejo-Siguan, M.; Hofstetter, Y. J.; Cho, C.; Paulus, F.; Grancini, G.; Vaynzof, Y. 23.7% efficient inverted perovskite solar cells by dual interfacial modification. *Sci. Adv.* **2021**, *7*, No. eabj7930.

(23) Jiang, X.; Chen, S.; Li, Y.; Zhang, L.; Shen, N.; Zhang, G.; Du, J.; Fu, N.; Xu, B. Direct surface passivation of perovskite film by 4-fluorophenethylammonium iodide toward stable and efficient perovskite solar cells. *ACS Appl. Mater. Interfaces* **2021**, *13*, 2558−2565.

(24) Zhu, T.; Zheng, D.; Liu, J.; Coolen, L.; Pauporté, T. PEAI-based interfacial layer for high-efficiency and stable solar cells based on a MACl-mediated grown $FA_{0.94}MA_{0.06}PbI_3$ perovskite. *ACS Appl. Mater. Interfaces* **2020**, *12*, 37197−37207.

(25) Davies, C. L.; Borchert, J.; Xia, C. Q.; Milot, R. L.; Kraus, H.; Johnston, M. B.; Herz, L. M. Impact of the organic cation on the optoelectronic properties of formamidinium lead triiodide. *J. Phys. Chem. Lett.* **2018**, *9*, 4502−4511.

(26) Eperon, G. E.; Stranks, S. D.; Menelaou, C.; Johnston, M. B.; Herz, L. M.; Snaith, H. J. Formamidinium lead trihalide: a broadly tunable perovskite for efficient planar heterojunction solar cells. *Energy Environ. Sci.* **2014**, *7*, 982−988.

(27) Mu, C.; Pan, J.; Feng, S.; Li, Q.; Xu, D. Quantitative doping of chlorine in formamidinium lead trihalide ($FAPbI_{3-x}Cl_x$) for planar heterojunction perovskite solar cells. *Adv. Energy Mater.* **2016**, *7*, 1601297.

(28) Lee, J. W.; Seol, D. J.; Cho, A. N.; Park, N. G. High-efficiency perovskite solar cells based on the black polymorph of $HC(NH_2)_2PbI_3$. *Adv. Mater.* **2014**, *26*, 4991−4998.

(29) Manser, J. S.; Saidaminov, M. I.; Christians, J. A.; Bakr, O. M.; Kamat, P. V. Making and breaking of lead halide perovskites. *Acc. Chem. Res.* **2016**, *49*, 330−338.

(30) Zhou, Y.; Yang, M.; Pang, S.; Zhu, K.; Padture, N. P. Exceptional morphology-preserving evolution of formamidinium lead triiodide perovskite thin films via organic-cation displacement. *J. Am. Chem. Soc.* **2016**, *138*, 5535−5538.

(31) Kim, M.; Kim, G. H.; Lee, T. K.; Choi, I. W.; Choi, H. W.; Jo, Y.; Yoon, Y. J.; Kim, J. W.; Lee, J.; Huh, D.; Lee, H.; Kwak, S. K.; Kim, J. Y.; Kim, D. S. Methylammonium chloride induces intermediate phase stabilization for efficient perovskite solar cells. *Joule* **2019**, *3*, 2179−2192.

(32) Luo, P.; Zhou, S.; Zhou, Y.; Xia, W.; Sun, L.; Cheng, J.; Xu, C.; Lu, Y. Fabrication of $Cs_xFA_{1-x}PbI_3$ mixed-cation perovskites via gas-phase-assisted compositional modulation for efficient and stable photovoltaic devices. *ACS Appl. Mater. Interfaces* **2017**, *9*, 42708−42716.

(33) Haris, M. P. U.; Kazim, S.; Ahmad, S. Low-temperature-processed perovskite solar cells fabricated from presynthesized $CsFAPbI_3$ powder. *ACS Appl. Energy Mater.* **2021**, *4*, 2600−2606.

(34) Park, Y. H.; Jeong, I.; Bae, S.; Son, H. J.; Lee, P.; Lee, J.; Lee, C. H.; Ko, M. J. Inorganic rubidium cation as an enhancer for photovoltaic performance and moisture stability of $HC(NH_2)_2PbI_3$ perovskite solar cells. *Adv. Funct. Mater.* **2017**, *27*, 1605988.

(35) Gao, B.; Meng, J. $RbCs(MAFA)PbI_3$ perovskite solar cell with 22.81% efficiency using the precise ions cascade regulation. *Appl. Surf. Sci.* **2020**, *530*, 147240.

(36) Chavan, R. D.; Prochowicz, D.; Tavakoli, M. M.; Yadav, P.; Hong, C. K. Surface treatment of perovskite layer with guanidinium iodide leads to enhanced moisture stability and improved efficiency of perovskite solar cells. *Adv. Mater. Interfaces* **2020**, *7*, 2000105.

(37) Kubicki, D. J.; Prochowicz, D.; Hofstetter, A.; Saski, M.; Yadav, P.; Bi, D.; Pellet, N.; Lewiński, J.; Zakeeruddin, S. M.; Grätzel, M.;

https://doi.org/10.1021/acsomega.2c03976
ACS Omega 2022, 7, 37359−37368

Emsley, L. Formation of stable mixed guanidinium-methylammonium phases with exceptionally long carrier lifetimes for high-efficiency lead iodide-based perovskite photovoltaics. *J. Am. Chem. Soc.* **2018**, *140*, 3345−3351.
(38) Xia, Y.; Zhao, C.; Zhao, P.; Mao, L.; Ding, Y.; Hong, D.; Tian, Y.; Yan, W.; Jin, Z. Pseudohalide substitution and potassium doping in $FA_{0.98}K_{0.02}Pb(SCN)_2I$ for high-stability hole-conductor-free perovskite solar cells. *J. Power Sources* **2021**, *494*, 229781.
(39) Kim, M.; Lee, T. K.; Choi, I. W.; Choi, H. W.; Jo, Y.; Lee, J.; Kim, G. H.; Kwak, S. K.; Kim, D. S. Effects of cation size and concentration of cationic chlorides on the properties of formamidinium lead iodide based perovskite solar cells. *Sustainable Energy Fuels* **2020**, *4*, 3753−3763.
(40) Zhang, Y.; Li, Y.; Zhang, L.; Hu, H.; Tang, Z.; Xu, B.; Park, N. G. Propylammonium chloride additive for efficient and stable $FAPbI_3$ perovskite solar cells. *Adv. Energy Mater.* **2021**, *11*, 2102538.
(41) Li, Z.; Yang, M.; Park, J. S.; Wei, S. H.; Berry, J. J.; Zhu, K. Stabilizing perovskite structures by tuning tolerance factor: formation of formamidinium and cesium lead iodide solid-state alloys. *Chem. Mater.* **2016**, *28*, 284−292.
(42) Lee, J. W.; Kim, D. H.; Kim, H. S.; Seo, S. W.; Cho, S. M.; Park, N. G. Formamidinium and cesium hybridization for photo- and moisture-stable perovskite solar cell. *Adv. Energy Mater.* **2015**, *5*, 1501310.
(43) Yi, C.; Luo, J.; Meloni, S.; Boziki, A.; Ashari-Astani, N.; Grätzel, C.; Zakeeruddin, S. M.; Röthlisberger, U.; Grätzel, M. Entropic stabilization of mixed A-cation ABX_3 metal halide perovskites for high performance perovskite solar cells. *Energy Environ. Sci.* **2016**, *9*, 656−662.
(44) Pham, H. T.; Yin, Y.; Andersson, G.; Weber, K. J.; Duong, T.; Wong-Leung, J. W. Unraveling the influence of CsCl/MACl on the formation of nanotwins, stacking faults and cubic supercell structure in FA-based perovskite solar cells. *Nano Energy* **2021**, *87*, 106226.
(45) Chavan, R. D.; Prochowicz, D.; Yadav, P.; Tavakoli, M. M.; Nimbalkar, A.; Bhoite, S. P.; Hong, C. K. Effect of CsCl additive on the morphological and optoelectronic properties of formamidinium lead iodide perovskite. *Sol. RRL* **2019**, *3*, 1900294.
(46) Prochowicz, D.; Runjhun, R.; Tavakoli, M. M.; Yadav, P.; Saski, M.; Alanazi, A. Q.; Kubicki, D. J.; Kaszkur, Z.; Zakeeruddin, S. M.; Lewiński, J.; Grätzel, M. Engineering of perovskite materials based on formamidinium and cesium hybridization for high-efficiency solar cells. *Chem. Mater.* **2019**, *31*, 1620−1627.
(47) Matondo, J. T.; Malouangou, M. D.; Bai, L.; Yang, Y.; Zhang, Y.; Mbumba, M. T.; Akram, M. W.; Guli, M. Improving the properties of MA-based wide-bandgap perovskite by simple precursor salts engineering for efficiency and ambient stability improvement in solar cells. *Sol. Energy Mater. Sol. Cells* **2022**, *238*, 111617.
(48) Lyu, M.; Park, N. G. Effect of additives AX (A = FA, MA, Cs, Rb, NH_4, X = Cl, Br, I) in $FAPbI_3$ on photovoltaic parameters of perovskite solar cells. *Sol. RRL* **2020**, *4*, 2000331.
(49) Imran, M.; Khan, N. A. Perovskite phase formation in formamidinium−methylammonium lead iodide bromide $(FAPbI_3)_{1-x}(MAPbBr_3)_x$ materials and their morphological, optical and photovoltaic properties. *Appl. Phys. A* **2019**, *125*, 575.
(50) Zhang, X.; Qiu, W.; Song, W.; Hawash, Z.; Wang, Y.; Pradhan, B.; Zhang, Y.; Naumenko, D.; Amenitsch, H.; Moons, E.; Merckx, T.; Aguirre, A.; Abdulraheem, Y.; Aernouts, T.; Zhan, Y.; Kuang, Y.; Hofkens, J.; Poortmans, J. An integrated bulk and surface modification strategy for gas-quenched inverted perovskite solar cells with efficiencies exceeding 22%. *Sol. RRL* **2022**, *6*, 2200053.

https://doi.org/10.1021/acsomega.2c03976
ACS Omega 2022, 7, 37359−37368